2025-sCO2.eu-196

AN INVESTIGATION OF SUPERCRITICAL CARBON DIOXIDE IN 1.5 MM HORIZONTAL CHANNELS AT ELEVATED THERMAL LOADS

Zachary Jackson
Oxford Thermofluids Institute
Oxford, United Kingdom
Email: zachary.jackson@eng.ox.ac.uk

Peter Ireland
Oxford Thermofluids Institute
Oxford, United Kingdom

ABSTRACT

The Oxford Laser Heating Facility (OLAHF) has been upgraded with a supercritical carbon dioxide (sCO_2) flow circulating loop, capable of providing component level flow rates to test pieces at temperatures and pressures up to 100°C and 100 bar. Near to the critical point, the large variations in sCO_2 thermophysical properties can lead to adverse cooling and heat transfer effects. There are currently gaps in the understanding of the effects of larger thermal gradients (i.e. heat fluxes) on the heat transfer performance of sCO_2 systems. An initial experimental campaign was performed on an additively manufactured stainless steel test piece containing an array of 11, 1.5 mm square internal channels using the high power laser modules located at OLAHF. Heat fluxes ranging from 116 to 1000 kW/m^2 to the upper surface of the horizontally-oriented test piece. Data were obtained for fluid inlet temperatures between 18 and 28°C and mass fluxes of 1500 and 3000 kg/m^{2}s at a constant inlet pressure of 80 bar (inlet Reynolds numbers from 3 x 10^4 to 8 x 10^4). Resulting heat transfer coefficients were determined using a combination of ray tracing and finite element (FE) analyses of the test piece at each experimental condition. Average heat transfer coefficients were shown to exhibit a significant dependence on applied heat flux for both mass flux conditions and all inlet temperatures. The heat transfer coefficients were compared to empirical correlations with varied levels of agreement. The data was additionally examined for the potential existence of buoyancy and flow acceleration effects.

INTRODUCTION

Supercritical carbon dioxide (sCO_2) has become a major research focus on account of its potential as a working fluid in power cycles and for application in heat exchangers tasked with managing the heat loads associated with some of the most extreme thermal conditions. Current research activity ranges from cooling micro-electronics [1] to nuclear fusion reactors [2] and concentrated solar power plants [3].

CO_2 exhibits large variations in thermophysical properties at and above its critical pressure (73.8 bar), as seen in Fig. 1. This leads to a significant spike in Prandtl number – a useful

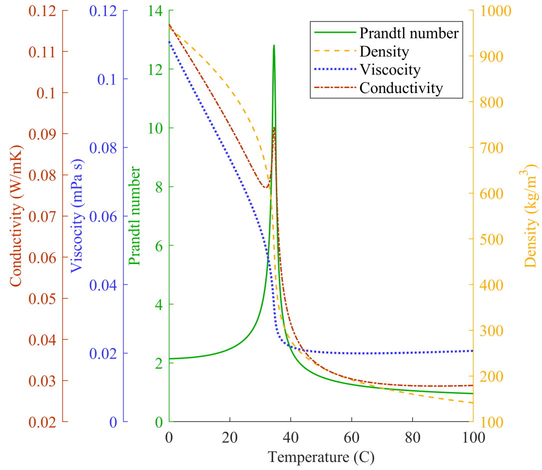

Figure 1: Temperature dependence of CO_2 thermophysical properties at P = 80 bar [4].

indicator of the thermal transport capability of a fluid – that is coupled with a rapid decrease in density ρ as temperatures pass through the *pseudo*critical temperature T_{pc}, the temperature where the specific heat capacity at constant pressure is largest for a given pressure.

The strong non-uniformity of sCO_2's fluid properties drives unique heat transfer phenomena macroscale, uniformly heated flow geometries [5]. Deteriorated heat transfer (DHT), driven by buoyancy or bulk flow acceleration, or by a combination of the two, results when relaminarisation of the turbulent boundary layer occurs [6]. Increasing thermal loads reverses the negative heat transfer trend as turbulence production becomes driven by buoyancy and natural convection, resulting in a recovery in heat transfer performance and a further distortion of the velocity profile. These heat transfer characteristics are present in both horizontal [7] and upward vertical flows [8], and are consistent across various tube cross sections, both circular and non-circular [9].

More recent studies have been undertaken [10, 11] to address a lack of understanding in how reported correlations and DHT screening criteria apply cases of non-uniform heating of horizontal flows. However, the total volume of work is this area is limited and there remains significant uncertainty

DOI: 10.17185/duepublico/83308

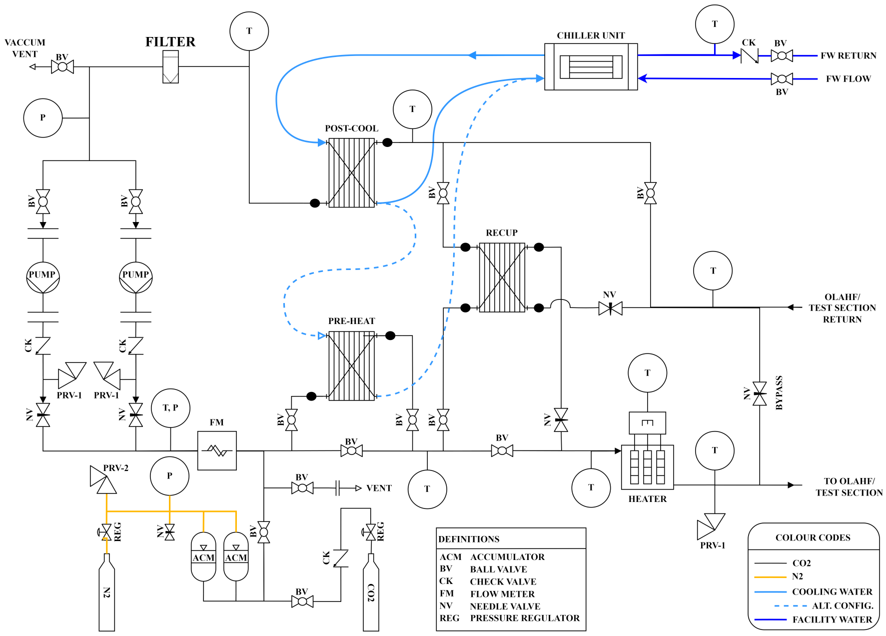

Figure 2: Schematic of the OLAHF CO_2 conditioning loop.

in the applicability of past research to such cases. Further, heat transfer behaviour of sCO_2 has only been investigated at relatively low heat fluxes q to date, and there is a lack of data where heat flux levels are high (q >500 kW/m^2). Increases in q for a given inlet condition leads to higher wall temperatures, which would be expected to increase the magnitude of DHT effects present and result in the earlier onset of both DHT and post-DHT recovery. This study investigates five heat fluxes (q = 116, 232, 400, 800, 1000 kW/m^2) that are applied non-uniformly to a horizontally-oriented test piece using the laser system present at the Oxford Laser Heating Facility (OLAHF). Heat transfer performance is investigated at two mass fluxes (G = 1500 and 3000 kg/m^{2}s) at a constant pressure of 80 bar and inlet temperatures from 18 to 28°C.

EXPERIMENTAL FACILITIES

A supercritical carbon dioxide system capable of providing component-level sCO_2 flow rates – at temperatures and pressures ranging from 20 to 100 °C and 80 to 100 bar – has been installed at the Oxford Laser Heating Facility [12]. A schematic of the new facility is given in Fig. 2.

Two side-channel pumps[1] operating in parallel drive the flow to the test piece. Each pump is independently capable of providing a flow rate of 400 g/s at a dynamic head of 60 metres for inlet pressures up to 110 bar. Loop pressures are set and maintained above the critical pressure by piston accumulators connected to a 230 bar nitrogen supply.

Three brazed plate heat exchangers[2] provide both heating and cooling capability and enable high test temperatures at large sCO_2 flow rates. A water cooling loop controlled by a chiller unit[3] provides 30 kW of cooling power and is controlled to ensure the CO_2 returns to the pumps in a liquid-like state ($T \leq 20$°C). It is connected to the main facility's primary cooling water circuit, which provides a constant supply of 6°C water. An 18.4 kW in-line circulation heater[4] provides the main heat input and is used to set test section inlet temperature.

Temperatures are measured around the loop using standard type-T thermocouples (base uncertainty of ±0.5°C or 0.4%), while pressures are monitored at either side of the pump via pressure transducers[5] with an operating range of 0 to 160 bar and nominal accuracy of 0.5% full span. Flow rates are measured by a Coriolis flow meter[6] with a range of 0 to 100 kg/min and a base uncertainty of ±0.2%. These measurements are incorporated into the facility's existing data acquisition setup[7], driven by a LabVIEW-architecture control system that manages the input and output signals to the pumps, lasers, and heater while providing continuous live data readings.

The experimental test section is located within the experimental laser area. The pressure differential between its inlet and outlet is measured by a differential pressure transducer[8] with a range of 0 - 3 bar and base accuracy of 0.049%.

Test Piece

A test piece with an array of 11, 1.5 mm square channels (aspect ratio of 1) was manufactured from 316 stainless steel (UNS S31600) via direct laser metal sintering (DMLS). A schematic of the instrumented test piece is shown in Fig. 3, with the experimental setup shown in Fig. 4.

[1] Dickow Pumpen WPM25; https://www.dickow.de/
[2] SWEP B18 series; https://www.swep.net/
[3] Custom unit; https://riedel-kooling.com/
[4] CAST-X 3000; https://www.castaluminumsolutions.com/
[5] Swagelok PTI-S-AG160
[6] Rheonik RHM12L; https://www.rheonik.com/
[7] National Instruments cDAQ-1989; https://www.ni.com/
[8] Endress+Hauser Deltabar PMD55B; https://www.endress.com/

DOI: 10.17185/duepublico/83308

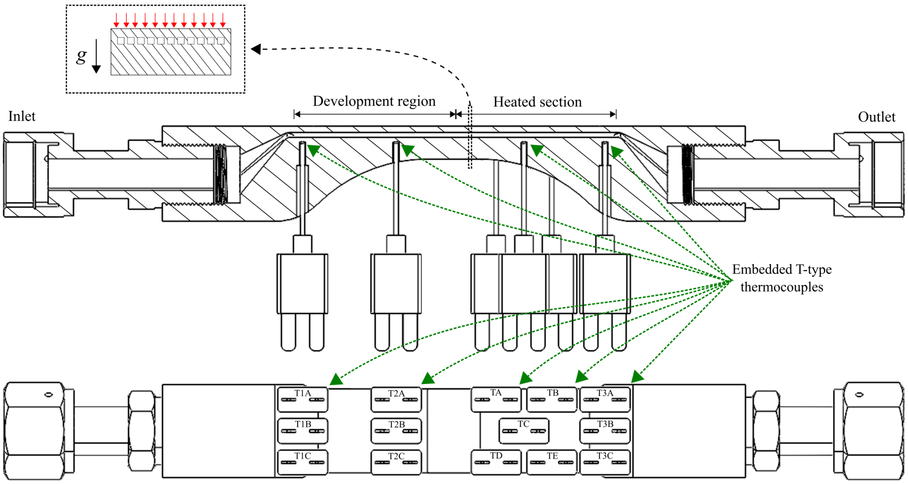

Figure 3: Section (top) and bottom views (below) of the experimental test piece showing the internal channel and instrumentation structure as well as thermocouple labelling pattern.

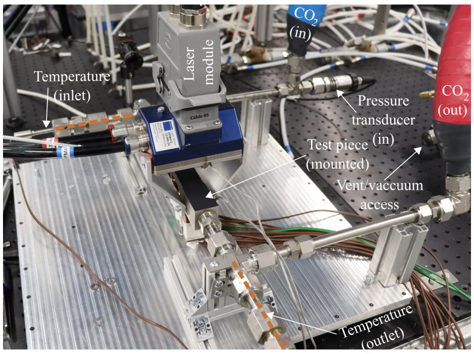

Figure 4: The experimental section, showing a mounted test piece and laser module.

Test piece channel length L was 106 mm, with a 53 mm (35D) flow development region upstream of the 53 mm length heated region. Temperature measurements were taken 1.5 mm from the fluid path using Class 1 type-T thermocouples (base uncertainty ± 0.25°C) that were mounted and fixed using AS1802 SILCOTHERM® at 14 locations along the length of the channel at non-dimensional locations l/L of 0.037, 0.33, 0.63, 0.73, 0.82, 0.98. The top surface was coated with a high-emissivity paint[9] to ensure the absorption of the applied laser remained consistent. This coating was previously calculated to have an absorption coefficient α of 0.87 ± 0.012 [12].

NUMERICAL APPROACH

A combination of ray tracing and finite element analyses were used in this study to evaluate the experimental conditions. The basis of each method, and its respective interaction with the others, is described in the following section. Supporting computational fluid dynamics (CFD) simulations were also performed, with details of these studies to be published in the near future. These studies used the k-ω shear stress transport turbulence model, with fluid properties taken from NIST [4].

Ray Tracing

Ray tracing was performed in LightTools® version 8.5.0 on a computer-generated representation of the experimental test section (see Fig. 4) to create a numerical representation of the applied experimental heat flux. This modelling technique has been demonstrated to reproduce experimentally applied heat fluxes with a high degree of accuracy [12].

A total of 10 million ray paths were modelled using a Monte Carlo simulation method, resulting in the normalised intensity distribution shown in Fig. 5. This distribution was scaled by the absorptivity of the top coating and the ratio of applied to maximum laser power for each heat flux investigated.

Finite element analyses

FE simulations of the symmetric solid domain were performed in ANSYS Mechanical 23.1. Temperature dependent thermophysical properties of 316 steel were taken from [13]. A mesh independence study set the sizes of the fluid-solid interface to 0.25 mm. The surface mesh was matched to the ray tracing profile data (0.5 mm) to minimize interpolation errors, resulting in 228798 computational elements.

Convective heat transfer coefficients were applied to the faces in contact with the sCO_2 and were referenced to a bulk temperature that varied along the length of the channel as shown in Fig. 6. These distributions were taken from supporting computational fluid dynamics (CFD) simulations which are not included in this current paper. The same heat transfer coefficient h was used on all internal faces of the square cross-section channels. This represents an average value and allows for direct comparison to previous studies of microchannel geometries. Further boundary conditions were also applied: natural convection and radiative heat losses

[9] Aremco HiE-Coat™ 840-CM

DOI: 10.17185/duepublico/83308

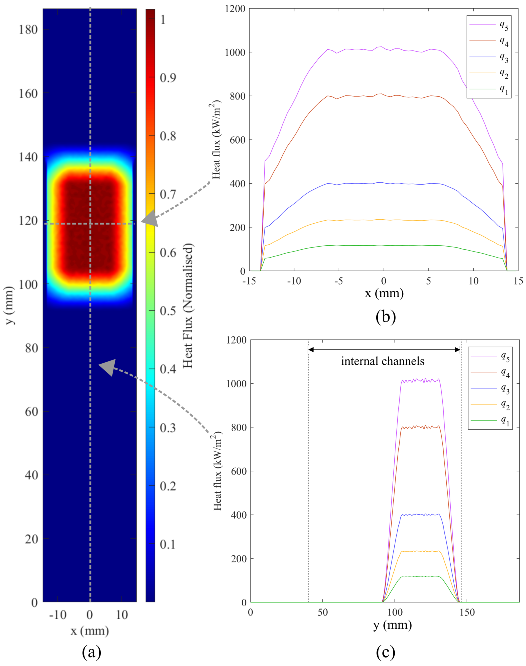

Figure 5: The predicted and normalised heat flux spatial distribution present on the top of the test piece (a) next to each experimental heat flux level along the lines y = 120 mm (b) and x=0 (c) with respect to test piece dimensions.

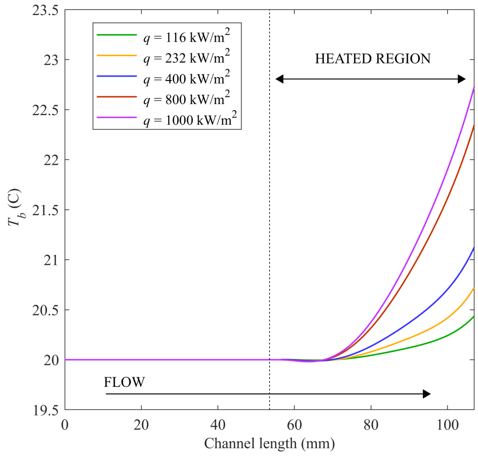

Figure 6: CFD-generated bulk temperature profiles for each experimental heat flux at an experimental mass flux of G = 1500 kg/m^{2}s and inlet temperature of 20 °C.

from the external surfaces of the test piece, and conduction heat loss to the experimental test loop.

A database of FE-generated temperatures was created for a range of heat transfer coefficients at each heat flux and flow rate investigated. This is depicted in Fig. 7, where experimental values of T_C are superimposed alongside the FE-predicted values at constant values of h, for the case where q = 400 kW/m^2 and G = 1500 kg/m^{2}s.

The resulting heat transfer performance characteristics of the experimental system were then determined by reverse interpolation, where each temperature measurement in the

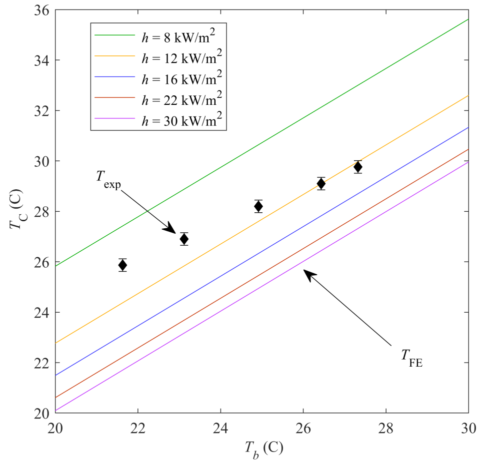

Figure 7: Experimental temperatures at point T_C as a function of T_b plotted alongside FE-generated temperatures at the same location for constant values of h for the experimental condition with q = 400 kW/m^2 and G = 1500 kg/m^{2}s.

heated region of the test piece was an input. The resulting calculated heat transfer coefficients corresponding to each specific temperature location (h_{T_A}, h_{T_B}, h_{T_C}, etc) were then averaged together to create a unified value for each test point.

Uncertainty analysis

A combined small perturbation and finite difference approach prescribed by Taylor [14] was used to calculate the uncertainties in this study. The total uncertainty percentage U_{tot} in heat transfer coefficient h resulting from this analysis are calculated using a root-sum-square method:

$$U_{tot} = \sqrt{\sum_{i=1}^{N} (U_i)^2} \tag{1}$$

$$U_i = \left(\frac{\delta h}{\delta \chi_i}\right) \frac{\Delta \chi_i}{h_c} \tag{2}$$

where individual percentages U_i from each source of uncertainty was calculated according to Eq. (2). The change in h relative to the source of the uncertainty is given by the partial derivative $\delta h / \delta \chi_i$ while $\Delta \chi$ is the magnitude of each uncertainty and h_c is the most likely (calculated) value for each case.

A sensitivity study was conducted to ascertain the relative effects of each boundary condition on the temperature distribution at discrete values of the channel heat transfer coefficient for the FE-based data reduction. Small changes to each condition – surface emissivity ϵ, conduction losses Q_{cond}, laser surface absorptivity α, inlet and outlet region heat transfer h_{in}, h_{out}, natural convection heat transfer h_{nat} – were made and the resulting differences in temperature recorded. The influence on the calculated experimental heat transfer coefficient was then included in the overall uncertainty value. Example calculations are given in Table 1.

DOI: 10.17185/duepublico/83308

Table 1: Example uncertainty calculations at the lowest and highest experimental heat fluxes for G = 1500 kg/m^{2}s.

	q = 116 kW/m^2			q = 1000 kW/m^2		
Parameter	**Typical Value**	$\delta h/\delta\chi$	U_i	**Typical Value**	$\delta h/\delta\chi$	U_i
T_{exp}	28.33 (C)	6.2x10^3	0.14	36.21 (C)	929	0.0191
$h_{nat,\text{FE}}$	50 (W/m^{2}K)	-37	-0.086	100 (W/m^{2}K)	-5	-0.01
$h_{in,\text{FE}}$	1000 (W/m^{2}K)	-0.084	-0.0059	1000 (W/m^{2}K)	-0.011	-7.2x10^{-4}
$h_{out,\text{FE}}$	750 (W/m^{2}K)	-0.013	-0.0055	750 (W/m^{2}K)	-0.0018	-6.7x10^{-4}
$Q_{cond,\text{FE}}$	-3 (W)	113	0.053	-30 (W)	16.5	0.0068
ϵ_{FE}	0.9	-179	-0.0075	0.9	-24	-8.9x10^{-4}
α_{FE}	0.87	6.8x10^4	0.076	0.87	9.3x10^3	0.0091
U_{tot}			**19.35%**			**2.47%**

RESULTS AND DISCUSSION

Experiments were performed for the parameters listed in Table 2. The laser power was adjusted to apply the desired heat flux condition to the top surface of the test piece. Inlet temperatures were kept below T_{pc} and ranged from $18 \leq T_{in} \leq 28$°C ($T_{pc|80\text{bar}}$ = 34.65 C). Data was recorded at a frequency of 1 Hz for a minimum of 7 minutes after the system had reached steady-state, assessed as being reached once the variation in experimentally measured heat input with time was significantly less than the laser power input:

$$\dot{m}C_p\frac{dT}{dt} < \frac{Q}{1000} \tag{3}$$

The data collected over this period was then averaged to give a single value for each test set point resulting in 50 total data points.

Table 2: Experimental parameters.

Parameter	**Unit**	**Value**
Hydraulic diameter	mm	1.5
Flow orientation	-	Horizontal
Heat flux	kW/m^2	116, 232, 400, 800, 1000
Mass flux	kg/m^{2}s	1500, 3000
Inlet pressure	bar	80
Inlet temperature	°C	19 to 28

Heat transfer performance trends

Average experimental values of h are plotted against the ratio of bulk to pseudocritical temperature in Fig. 8, where the bulk temperature T_b is defined as the average of the inlet and outlet temperatures.

For all experimental heat and mass fluxes, there is a modest observable increase in heat transfer coefficient where T_b/T_{pc} <0.97 that broadly follows the increase in Prandtl number in this region.

For G = 1500 kg/m^{2}s and heat fluxes <400 kW/m^2, this trend is apparent over the full testing range. As T_b approaches T_{pc}, values of h increase by 20% from 9 to 10.75 kW/m^{2}K for q = 116 kW/m^2 and increase by 14% for q = 400 kW/m^2 (11.9 to 13.6 kW/m^{2}K). For applied heat fluxes $q \geq$400 kW/m^2, the trend reverses. Heat transfer coefficients reach maximum values of ~13 kW/m^{2}K at T_b/T_{pc} = 0.972 for both q = 800 and 1000 kW/m^2. As T_b increases above this, h then decreases by ~10% to be ~15% lower than the values where q = 400 kW/m^2.

In contrast, there is no decrease in h as T_b increases for the case when G = 3000 kg/m^{2}s: h increases by 32.7% (11.3 to 15 kW/m^{2}K) and 16% (15.3 to 17.8 kW/m^{2}K) for applied heat fluxes of q = 116 and 400 kW/m^2, respectively, while remaining relatively constant at the highest two heat fluxes. Overall, an increase in the mass flux of ~100% corresponds to an increase in h of only ~30% for each individual heat flux. This is less than what would otherwise be expected and is likely due to the effects brought about by the variable properties of sCO_2. The presence of these effects is discussed in subsequent sections.

The magnitude of applied heat flux also impacts the magnitude of h, as shown in Table 3. The trend is similar to the one found with increasing T_b: values of $\overline{h}$ increase where $q \leq$ 400 kW/m^2 for the low flow rate case, and consistently increase for the high flow case before a slight dip at the highest heat flux.

Table 3: The change in average heat transfer coefficient $\overline{h}$ as applied heat flux (in kW/m^2) is increased over the specified range (first column).

	$\Delta\overline{h}$ (%)	
Δq (kW/m^2)	**1500 kg/m^{2}s**	**3000 kg/m^{2}s**
116 → 232	17.90	15.55
232 → 400	12.61	14.89
400 → 800	-1.45	10.11
800 → 1000	-3.40	-0.94

Screening data for flow acceleration

As sCO_2 flows through a heated tube its bulk fluid density falls as its temperature rises. For a constant mass flow, the flow velocity must increase to fulfill continuity criteria; this creates an acceleration of the fluid axially along the length of the heated channel. Further, the acceleration in bulk velocity is linked to an expansion of the fluid as the density decreases. This flattens the velocity profile, influences the gradient of shear stresses in the flow and results in a case where they are lower in the buffer region than in a case with no acceleration. This subsequently reduces turbulence production that decreases heat transfer performance [5].

The relative effects of bulk flow acceleration have been correlated in a semi-empirical model [5] which expresses the ratio of Nusselt numbers $\text{Nu}_b/\text{Nu}_{b0}$, where Nu_b is the

DOI: 10.17185/duepublico/83308

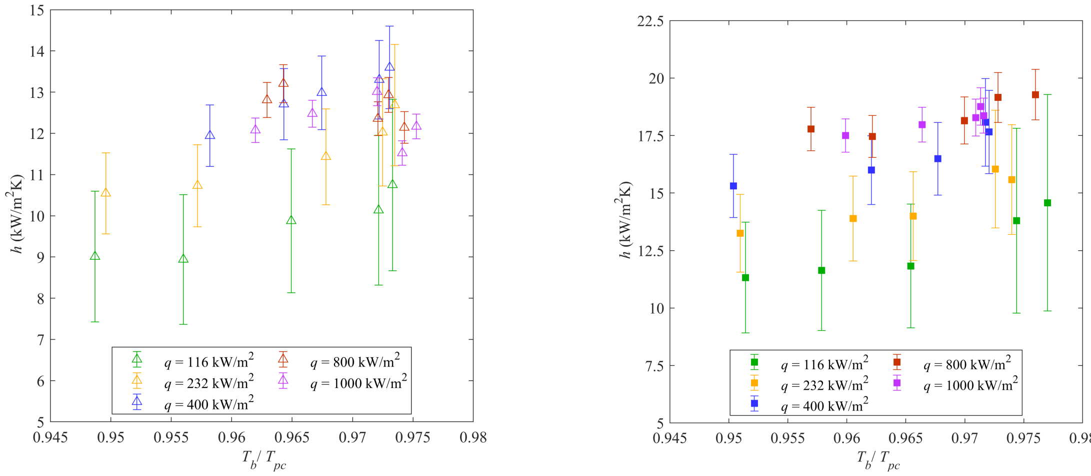

(a)

(b)

Figure 8: Average heat transfer coefficients plotted against T_b/T_{pc} for G = 1500 kg/m^{2}s (a) and G = 3000 kg/m^{2}s (b).

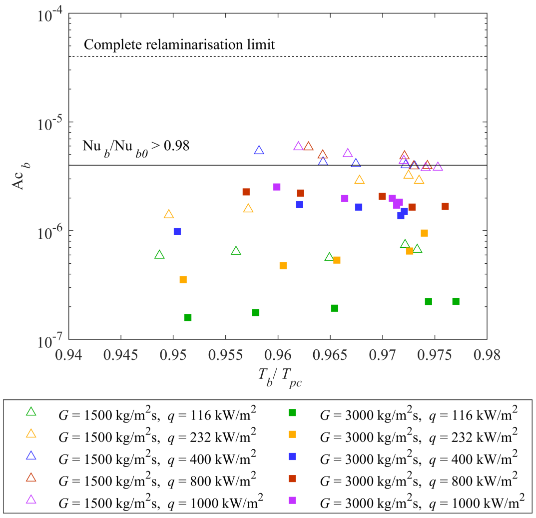

Figure 9: Calculated experimental acceleration parameter Ac_b plotted against the ratio of bulk to pseudocritical temperature T_b/T_{pc}. Also plotted are the relaminarisation limit and where heat deterioration effects are less than 2% [5].

Nusselt number where flow acceleration exists, and Nu_{b0} the Nusselt number where it does not: net effects of acceleration are less than 2% cf where parameter Ac_b <4x10^{-6}, with Ac_b defined as

$$\mathrm{Ac}_b = \frac{q\beta_b D}{k_b \mathrm{Re}_b^{1.625}\mathrm{Pr}_b} \tag{4}$$

$$\beta_b = \frac{1}{\rho_b}\frac{\rho_w - \rho_b}{T_w - T_b} \tag{5}$$

where ρ_w and ρ_b are sCO_2 density evaluated at the wall and bulk temperatures, respectively, D is the hydraulic diameter of the test piece, and k_b is the sCO_2 thermal conductivity at the bulk temperature. Reynolds and Prandtl numbers Re_b and Pr_b are evaluated at the bulk temperature. Values of Ac_b are shown in Fig. 9 plotted against T_b/T_{pc} for each experimental test point.

This model indicates that a majority of test conditions are not impacted by flow acceleration effects. Only the highest three heat fluxes have data points above the point where Ac_b >4x10^{-6}. However, these points are not matched to where experimental heat transfer coefficients decrease where T_b/T_{pc} >0.97. Thus it can be inferred that the decreases in heat transfer at the highest heat fluxes seen in this study are not due to bulk flow acceleration, assuming that presently used models are applicable to the current study.

Screening data for effects of buoyancy

A significant density gradient will be present in a horizontally oriented heated channel when a fluid system operates near the pseudocritical point. Using data from this study where q = 1000 kW/m^2: with heated top wall and bulk fluid temperatures T_w and T_b of 46.7 and 28 °C, the densities at the wall ρ_w and bulk ρ_b are 173 and 743 kg/m^3, respectively. This difference may lead to the development of stable (or unstable) flow stratification where a layer of low-density sCO_2 forms along the upper channel wall.

A stable low-density layer along the top wall may decouple from the high-density flow at the base of the channel. This will induce acceleration effects, as previous mentioned, but may also result in a significant decrease in heat transfer as buoyant forces strongly modify the distribution of shear stresses in the flow. Under very strong heating, the buoyant layer becomes unstable and induces secondary flows that enhance turbulence production, leading to recovery in the heat transfer performance of the system [5].

Several methods [8] have been proposed to assess the strength of the buoyant forces that develop during turbulent horizontal mixed convection. However, at present, there is no consensus on the most suitable criteria to use for a set geometry and thermal loading condition. The present study focuses on two methods that have been developed to assess data for the likely presence of buoyancy in horizontal chan-

DOI: 10.17185/duepublico/83308

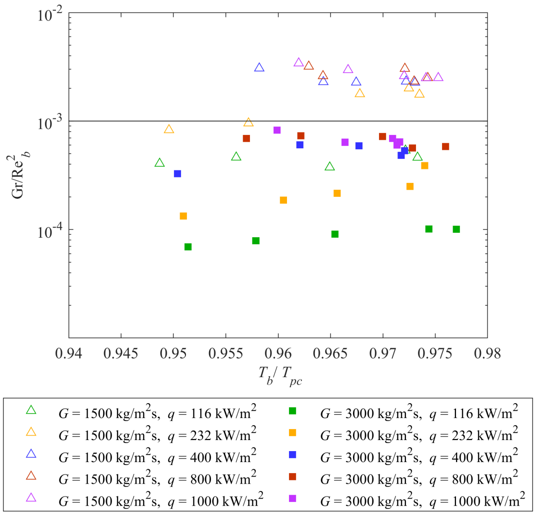

Figure 10: The calculated value of the Richardson number plotted against T_b/T_{pc}. Buoyancy effects should become negligible beneath black line.

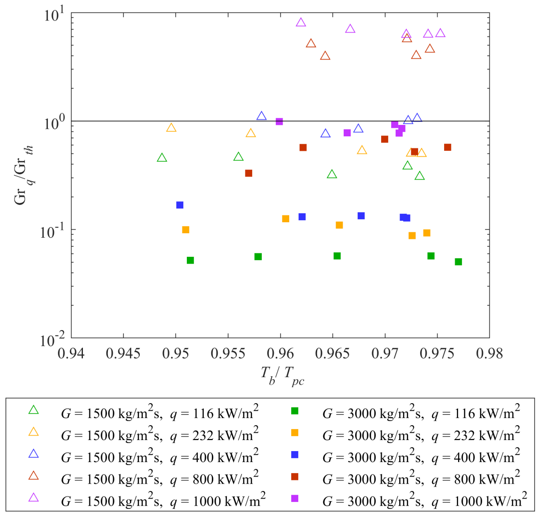

Figure 11: Ratio of Grashof numbers $\mathrm{Gr}_q/\mathrm{Gr}_{th}$ plotted against T_b/T_{pc}. Buoyancy effects should become negligible beneath black line.

nels. The first method assesses the value of the Richardson number, a ratio of natural convection to forced convection, whereby when

$$\frac{\mathrm{Gr}}{\mathrm{Re}_b^2} < 1\mathrm{x}10^{-3} \tag{6}$$

the effects of buoyancy on the heat transfer performance of the system will be negligible [15], where Gr is the Grashof number defined by

$$\mathrm{Gr} = \frac{g\rho_b D^3(\rho_w - \rho_b)}{\mu_b^2} \tag{7}$$

with μ_b the sCO_2 viscosity evaluated at the bulk temperature and g is gravity (9.81 m/s^2).

This ratio is plotted in Fig. 10 for each test condition, which illustrates that none of the experimental points for G = 3000 kg/m^2 are likely to be impacted by buoyancy driven effects. However, these effects are likely be present at most or all of the test points where G = 1500 kg/m^{2}s and q > = 116 kW/m^2.

The second method was developed by Petukhov and Polyakov [16] and involves a separate ratio of a heat flux-defined reformulation of the Grashof number Gr_q, defined as

$$\mathrm{Gr}_q = \frac{g\beta_{film} q \rho_b^2 D^4}{k_b \mu_b^2} \tag{8}$$

$$\beta_{film} = \frac{1}{\rho_{film}} \frac{\rho_b - \rho_w}{T_w - T_b} \tag{9}$$

where ρ_{film} is the density of the sCO_2 evaluated at average of the wall and bulk temperatures. These are related to a threshold Grashof number Gr_{th}

$$\mathrm{Gr}_{th} = 3\mathrm{x}10^{-5}\mathrm{Re}_b^{2.75}\overline{\mathrm{Pr}}\left[1 + 2.4\mathrm{Re}_b^{-\frac{1}{8}}\left(\overline{\mathrm{Pr}}^{\frac{2}{3}} - 1\right)\right] \tag{10}$$

with integrated Prandtl number $\overline{\mathrm{Pr}}$ defined as

$$\overline{\mathrm{Pr}} = \frac{i_w - i_b}{T_w - T_b}\frac{\mu_b}{k_b} \tag{11}$$

where i_w and i_b are the specific enthalpy values of sCO_2 at the wall and bulk, respectively. Where the ratio of these two Grashof numbers is equal to or less than 1, buoyancy effects should not be present.

Resulting ratio values for the present study are shown plotted in Fig. 11 against values of T_b/T_{pc}. The data indicate a smaller range of buoyancy influences on the data than Eq. (6): only the highest two heat fluxes (q = 800, 1000 kW/m^2) are likely to have buoyancy-related heat transfer deterioration effects. This provides good agreement with the heat transfer coefficient trends in Fig. 8.

Performance of empirical correlations

Experimental Nusselt numbers are compared to those predicted by several empirical correlations: Dittus-Boelter [17], Sieder-Tate [18], Liao-Zhao [7], Jackson-Hall [19], Kruizenga [20]. Details for each correlation are given in given in Table 4, and ratios of predicted-to-experimental Nusselt number $\mathrm{Nu}_{pred}/\mathrm{Nu}_{exp}$ are plotted against T_b/T_{pc} in Fig. 12. Performance of these correlations is assessed in Table 5 at each test point using the root mean square percentage error (RMSPE) calculated as:

$$\mathrm{RMSPE} = \sqrt{\frac{1}{N}\sum_{j=1}^{N}\left(\frac{\mathrm{Nu}_{\exp,j} - \mathrm{Nu}_{\mathrm{pred},j}}{\mathrm{Nu}_{\exp,j}}\right)^2} \tag{12}$$

The Dittus-Boelter and Sieder-Tate correlations are single phase forced convection heat transfer correlations, with the Sieder-Tate correlation providing better performance for systems where the non-uniformity of fluid properties at the wall is significant. Their performance is plotted in Fig. 12(a) and (b), respectively. Applied heat flux is the main influence

DOI: 10.17185/duepublico/83308

Table 4: Nusselt number correlations considered for comparison in this study.

Author (Year)	Correlation
Dittus and Boelter (1930) [17]	$\mathbf{Nu_{DB}} = 0.023\mathrm{Re}_b^{0.8}\mathrm{Pr}_b^{0.4}$
Sieder and Tate (1936) [18]	$\mathbf{Nu_{ST}} = 0.027\mathrm{Re}_b^{0.8}\mathrm{Pr}_b^{0.33}(\mu_b/\mu_w)^{0.14}$
	$\mathbf{Nu_{JH}} = 0.0183\mathrm{Re}_b^{0.82}\overline{\mathrm{Pr}}_b^{0.5}(\rho_w/\rho_b)^{0.3}(\overline{C}_p/C_{p,b})^n$
	$\overline{C}_p = (i_w - i_b)/(T_w - T_b)$
Jackson and Hall (1979) [19]	$n = 0.4, T_b < T_w < T_{pc}$
	$n = 0.4 + 0.3(T_w/T_{pc} - 1), T_b < T_{pc} < T_w$
	$n = 0.4 + 0.2(T_w/T_{pc} - 1)(1 - 5(T_w/T_{pc} - 1)), T_{pc} < T_b < 1.2T_{pc}$ with $T_b < T_w$
Liao and Zhao (2002) [7]	$\mathbf{Nu_{LZ}} = 0.124\mathrm{Re}_b^{0.8}\mathrm{Pr}_b^{0.4}(\mathrm{Gr}/\mathrm{Re}_b^2)^{0.203}(\rho_w/\rho_b)^{0.842}(\overline{C}_p/C_{p,b})^{0.384}$
Kruizenga et al(2012) [20]	$\mathbf{Nu_{Kr}} = \mathrm{Nu_{JH}}(\overline{C}_p/C_{p,b-IG})^{-0.19}$

Table 5: RMSPE in Nusselt number for each prediction method across each experimental heat flux for $G_1 = 1500$ kg/m^{2}s, $G_2 = 3000$ kg/m^{2}s.

	RMSPE G_1,G_2 (%)					
Correlation	q **= 116 kW/m^2**	**232 kW/m^2**	**400 kW/m^2**	**800 kW/m^2**	**1000 kW/m^2**	**Average**
Dittus-Boelter [17]	18.00, 14.93	29.27, 4.03	35.05, 12.71	33.07, 19.75	30.43, 19.07	29.16, 14.10
Sieder-Tate [18]	9.00, 50.30	3.85, 34.82	3.48, 29.02	5.70, 21.78	9.42, 23.28	6.29, 31.84
Jackson-Hall [19]	8.64, 29.81	13.94, 20.43	25.18, 8.52	41.07, 19.97	44.74, 26.17	26.71, 20.98
Liao-Zhao [7]	5.44, 3.28	42.82, 23.00	47.55, 45.77	30.22, 27.07	26.88, 21.42	30.58, 24.11
Kruizenga et al [20]	31.28, 6.26	41.22, 16.19	51.89, 30.13	58.91, 46.11	60.15, 48.80	48.69, 29.50

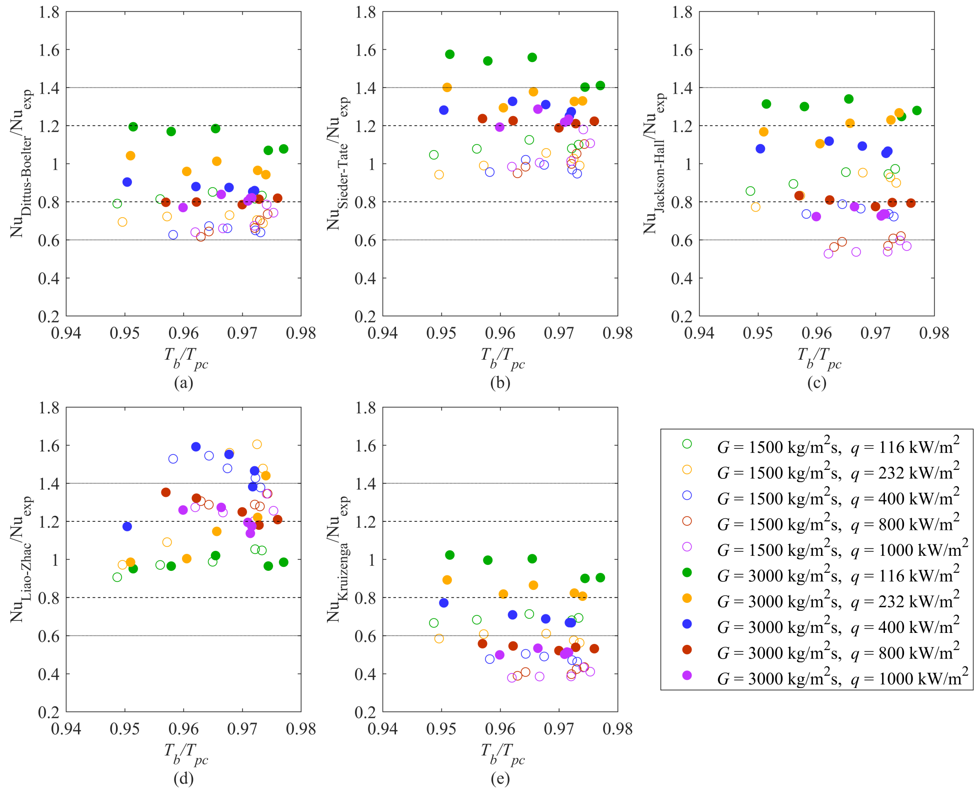

Figure 12: Ratios of predictions provided by the Nusselt number correlations given in Table 4 to experimental results (Dittus-Boelter (a), Sieder-Tate (b), Jackson-Hall (c), Liao-Zhao (d), Kruizenga et al (e)) against T_b/T_{pc}.

on the performance of each, with Dittus-Boelter accuracy decreasing as heat flux is increased and the opposite being true for the Sieder-Tate. The inclusion of the additional viscosity ratio (μ_b/μ_w) term in the Sieder-Tate correlation significantly improves its accuracy at high heat fluxes, decreases average RMSPE to only 6.29%. Neither shows much dependence on T_b/T_{pc}.

The Liao-Zhao [7], Jackson-Hall [19], Kruizenga [20] were developed specifically for supercritical fluids undergoing forced mixed convection. Each use the same basic principal applied in the Sieder-Tate correlation, including

 DOI: 10.17185/duepublico/83308

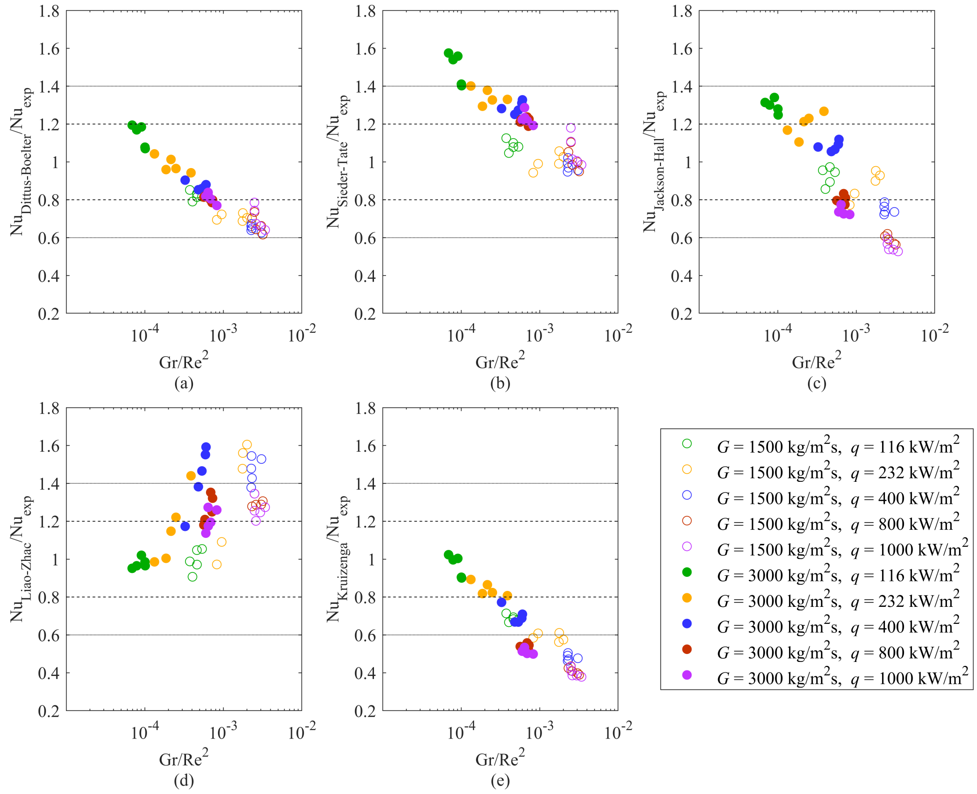

Figure 13: Ratios of predictions provided by the Nusselt number correlations given in Table 4 to experimental results (Dittus-Boelter (a), Sieder-Tate (b), Jackson-Hall (c), Liao-Zhao (d), Kruizenga et al (e)) plotted against Gr/Re^2.

additional thermophysical property ratio modifiers are added to account for the large differences in fluid properties present in the system. They're plotted in Fig. 12(c-e).

The Kruizenga et al. [20] correlation, in Fig. 12(e), is inaccurate at the highest heat fluxes investigated. Given it was developed for a system where sCO_2 was *cooled* rather than heated, that the magnitude of the under-prediction increases with heat flux is as would be expected. The Jackson and Hall correlation [19], plotted in Fig. 12(c), is more accurate, but still performs worse than the Dittus-Boelter correlation. Agreement is best at a limited combination of conditions, nominally where q is and G is high.

The single phase correlations, the Kruizenga, and Jackson and Hall correlations all fail to capture the trend in h presented in Fig. 8 and indeed predict its opposite: heat transfer coefficients that *decrease* as heat flux increases. The Liao-Zhao correlation [7] is the only correlation to adequately capture the experimental trend, although it has slightly higher RMSPE values than the Jackson-Hall correlation. In addition, the Liao-Zhao correlation appears to become more accurate across all q and G as T_b/T_{pc} increases.

The ratio of predicted-to-experimental Nusselt number Nu_{pred}/Nu_{exp} is plotted against the corresponding value of Gr/Re^2 in Fig. 13 to assess whether the observed discrepancies in Nusselt number are related to increases in the effects of buoyancy present in the system. Indeed, for all correlations except Liao-Zhao (which includes Gr/Re^2 in its formulation) as Gr/Re^2 increases Nu_{pred}/Nu_{exp} decreases linearly. Further, with the exception of the Sieder-Tate correlation, inaccuracy is highest where Gr/Re^2 > 1 x 10^{-3} suggesting that even the supercritical fluid correlations, despite being modified to account for thermophysical property variation, are unable to adequately characterise the heat transfer behaviour of the system when buoyancy effects are indicated to be present. As heat transfer performance of the system is being under-predicted, it is likely that the system heat transfer performance is in actuality being aided by the presence of the buoyancy at the highest applied heat fluxes and lowest flow rates rather than inhibited.

CONCLUSIONS

The heat transfer performance of sCO_2 has been investigated at the Oxford Laser Heating Facility (OLAHF) across a range of heat and mass fluxes. A horizontally-oriented test piece with an array of 11, 1.5 mm square channels was exposed to laser-applied heat fluxes of 116, 232, 400, 800, 1000 kW/m^2, which are among the highest that have been studied to date. Flow conditions were fixed at a pressure of 80 bar and at mass fluxes of 1500 and 3000 kg/m^{2}s, with sCO_2 inlet temperatures between 18 and 28°C (0.94< T_b/T_{pc} <0.98).

Heat transfer coefficients increased in a manner consistent with the increase in Prandtl number as T_b/T_{pc} increases while q < 400 kW/m^2. Heat transfer coefficients were also found to increase with heat flux for both G = 1500 and 3000 kg/m^2 where q < 800 kW/m^2. Above 800 kW/m^2 the trend is reversed and heat transfer performance decreased. The

DOI: 10.17185/duepublico/83308

location of the maximum value of h was found to shift to $T_b/T_{pc} = 0.97$ as applied heat flux increased, rather than the expected value of 1.

The Richardson number and a ratio of Grashof numbers given by Petukhov and Polyakov were used to assess the presence of buoyancy-influenced heat transfer. Both methods were found to be in agreement and indicated that buoyancy effects were present only where $G = 1500$ kg/m^2 and $q \geq 800$ kW/m^2. This broadly matched the trends seen in experimental data: heat transfer performance only remained steady at these heat fluxes where $T_b/T_{pc} < 0.97$, and was inferior to the condition where $q = 400$ kW/m^2.

Impacts on heat transfer resulting from bulk flow acceleration were also assessed. Where $q < 400$ kW/m^2, the effects on Nusselt number were estimated to be minimal, and only where $G = 1500$ kg/m^{2}s and $q > 400$ kW/m^2 were acceleration effects expected to be present. This observation matched the what was seen experimentally. Thus the decrease in h seen at the highest heat fluxes are likely to be solely due to a buoyant, low-density layer on the heated surfaces of the channels that limits heat transfer.

The Dittus-Boelter and Sieder-Tate correlations for single phase flows and the Jackson-Hall, Liao-Zhao, and Kruizenga correlations for supercritical fluid heat transfer were tested against the experimental data. No correlation provided consistent agreement over the range of test conditions, but performance was generally better where applied heat fluxes were lowest. The Liao-Zhao [7] correlation was the only method to match the broad experimental trends of increased, then decreased, h as heat flux increased. The inaccuracy of these correlations highlight the need for further investigation of non-uniform heating cases particularly at elevated heat flux levels where disagreement was highest.

Acknowledgements

This work was supported by Tokamak Energy Ltd and the (former) UK Department for Business, Energy, and Industrial Strategy as part of Advanced Modular Reactor Phase II programme. The support provided by Hal Surtell, Bill Godfrey, and Alex Bebb of the Oxford Thermofluids Institute and Holt Wong of Qdot Technology Ltd is greatly acknowledged.

REFERENCES

[1] B. M. Fronk and A. S. Rattner, "High-flux thermal management with supercritical fluids," *Journal of Heat Transfer*, vol. 138, pp. 1–4, 2016.

[2] J. Hidalgo-Salaverri, P. Cano-Megias, R. Chacartegui, J. Ayllon-Guerola, and E. Viezzer, "Analysis of supercritical carbon dioxide brayton cycles for a helium-cooled pebble bed blanket demo-like fusion power plant," *Fusion Engineering and Design*, vol. 173, 12 2021.

[3] Y. Liu, Y. Wang, and D. Huang, "Supercritical co2 brayton cycle: A state-of-the-art review," *Energy*, vol. 189, 12 2019.

[4] E. W. Lemmon, M. L. Huber, and M. O. McLinden, "Nist standard reference database 23: Reference fluid thermodynamic and transport properties-refprop, version 9.1," *National Institutes of Standards and Technology*, 2017.

[5] J. D. Jackson, "Fluid flow and convective heat transfer to fluids at supercritical pressure," *Nuclear Engineering and Design*, vol. 264, pp. 24–40, 2013.

[6] D. M. McEligot, C. W. Coon, and H. C. Perkins, "Relaminarization in tubes," *International Journal of Heat and Mass Transfer*, vol. 13, pp. 431–433, 1970.

[7] S. M. Liao and T. S. Zhao, "An experimental investigation of convection heat transfer to supercritical carbon dioxide in miniature tubes," *International Journal of Heat and Mass Transfer*, vol. 45, pp. 5025–5034, 2002.

[8] J. D. Jackson, "Models of heat transfer to fluids at supercritical pressure with influences of buoyancy and acceleration," *Applied Thermal Engineering*, vol. 124, pp. 1481–1491, 2017.

[9] J. K. Kim, H. K. Jeon, and J. S. Lee, "Wall temperature measurement and heat transfer correlation of turbulent supercritical carbon dioxide flow in vertical circular/non-circular tubes," *Nuclear Engineering and Design*, vol. 237, pp. 1795–1802, 2007.

[10] S. A. Jajja, K. R. Zada, and B. M. Fronk, "Experimental investigation of supercritical carbon dioxide in horizontal microchannels with non-uniform heat flux boundary conditions," *International Journal of Heat and Mass Transfer*, vol. 130, pp. 304–319, 2019.

[11] S. A. Jajja, J. M. Sequeira, and B. M. Fronk, "Geometry and orientation effects in non-uniformly heated microchannel heat exchangers using supercritical carbon dioxide," *Experimental Thermal and Fluid Science*, vol. 112, p. 109979, 2020.

[12] Z. Jackson, A. Bebb, P. Ireland, and J. Nicholas, "Combining high power laser modules with compound parabolic concentrators to test components at high heat fluxes," *Applied Thermal Engineering*, vol. 250, p. 123383, 2024.

[13] "Appendix A , Materials Design Limit Data," *ITER Structural Criterion for in – vessel components (SDC-IC)*, 2013.

[14] J. Taylor, *An Introduction to Error Analysis*. University Science Books, 2 ed., 1997.

[15] S. Kakaç, R. Shah, and W. Aung, *Handbook of Single-phase Convective Heat transfer*. Wiley, 1987.

[16] B. S. Petukhov, A. F. Polyakov, and B. E. Launder, "Heat transfer in turbulent mixed convection," 1988.

[17] F. W. Dittus and L. M. K. Boelter, "Heat transfer in automobile radiators of the tubular type," *University of California Publications in Engineering*, vol. 2, pp. 443–461, 1930.

[18] E. Sieder and G. Tate, "Heat transfer and pressure drop of liquids in tubes," *Industrial and Engineering Chemistry*, vol. 28, pp. 1429–1435, 1936.

[19] J. Jackson and W. B. Hall, "Forced convection heat transfer to fluids at supercritical pressure," *Turbulent Forced Convection in Channels and Bundles*, vol. 2, pp. 563–611, 1979.

[20] A. Kruizenga, H. Li, M. Anderson, and M. Corradini, "Supercritical carbon dioxide heat transfer in horizontal semicircular channels," *Journal of Heat Transfer*, vol. 134, 2012.

DOI: 10.17185/duepublico/83308

Published in: 6th European Conference on Supercritical CO2 (sCO2) for Energy Systems

DOI: 10.17185/duepublico/83308
URN: urn:nbn:de:hbz:465-20250428-102818-8